A Novel Synthesis of $Fe_3O_4@SiO_2@Au@$Porous SiO_2 Structure for NIR Irradiation-Induced DOX Release and Cancer Treatment

Meng Yang[1], Wenhua Yang[1], Liang Chen[1], Mingjian Ding[1], Chenhao Li[1], and Dongliang Shi[1] (ORCID)

Abstract

Doxorubicin (DOX) alone or in combination has been widely used for numerous cancers, including breast, lung, bladder, and so on. In this article, a core/shell/shell structured $Fe_3O_4@SiO_2@Au@$porous SiO_2 particles for the drug delivery and release of DOX was demonstrated, with the aid of near-infrared irradiation. Fe_3O_4 was used to direct the transportation and delivery of the drug-loaded composite to the target tissues and organs under an external magnetic field, the first layer of SiO_2 was used for Au nanoparticle attachment, Au acted as the agent for light–thermal conversion, and the porous SiO_2 was used to load DOX. The morphology of the nanoparticles was studied by transmission electron microscopy, and the porous structure was characterized by N_2 adsorption/desorption curves. The drug delivery system displayed high drug loading capacity, and the release behavior was largely impacted by the environmental pH. Furthermore, the cytotoxicity of $Fe_3O_4@SiO_2@Au@$porous SiO_2 and DOX loaded $Fe_3O_4@SiO_2@Au@$porous SiO_2 was studied through in vitro 3-(4,5-Dimethylthiazol-2-yl)-2,5-diphenyltetrazolium bromide cell viability assay.

Introduction

Cancer has been one of the most devastating diseases nowadays, which has resulted in millions of death all over the world each year.[1-4] At the current stage, there are still many huge challenges for the treatment of various cancers. Chemotherapy has been considered as an effective method to treat cancers.[5-7] Among the drugs used for chemotherapy treatment, doxorubicin (DOX) alone or in combination has been widely used for numerous cancers, including breast, lung, bladder, and so on.[8-14] Doxorubicin can intercalate into DNA and prevent the macromolecular biosynthesis and the growth of cancer cells.[15] However, the side effect of chemotherapy includes high toxicity and damages to healthy tissues and organs. Moreover, another difficulty with conventional chemotherapy is to accumulate chemotherapeutic agents within the cancer tissue and exert the treatment specifically for cancer cells.[15]

To solve this problem, the drug delivery system has been proposed and applied to accumulate drugs within the cancer tissues.[16-22] During the past decades, various nanoparticle-based drug delivery systems incorporating Au nanoparticles have been reported.[23] Within these systems, Au nanoparticles

are sensitive to light and display superb light–thermal conversion ability, which makes them a great candidate for light-induced drug release.[23] Different Au nanostructures that absorb near-infrared (NIR) irradiation have been synthesized, including nanorods, nanocages, nanostars, and so on, and have been prepared.[24] These structures have shown the capabilities of penetrating deep tissues for NIR-induced drug release. For example, Liu et al delivered Au nanoparticle-functioned peptides with loaded drugs to liver cancer cells and investigated the drug release under NIR.[25] Besides, Au nanoparticle-decorated liposomes and polyelectrolytes with various drug lodgings

[1] The Second Department of Thyroid and Breast Surgery, Cangzhou Central Hospital, Cangzhou, China

Corresponding Author:
Dongliang Shi, The Second Department of Thyroid and Breast Surgery, Cangzhou Central Hospital, Cangzhou, China.
Email: dongliangshiedu@protonmail.com

have been synthesized and applied for drug delivery and release.[26-30] However, the size of most of these capsules is too large for in vivo testing, which limits their further applications within biomedical fields.[31-34]

In this report, we synthesized a novel nanosized Fe_3O_4@SiO_2@Au@porous SiO_2 structure as a drug carrier. Fe_3O_4, SiO_2, and Au all possess low toxicity and high biocompatibility, which make them safe to be used within human organ tissues. The magnetization from Fe_3O_4 could be used to direct the drug delivery with the aid of an external magnetic field. Due to the inert surface of Fe_3O_4, another layer of SiO_2 layer was coated so that Au nanoparticles could be attached. The Au nanoparticles could generate heat within the structure under irradiation due to its superb light–thermal conversion ability. A final layer of porous SiO_2 was coated to prevent the detachment of Au nanoparticles and load drugs. A porous structure was able to provide a large surface area for drug loading. The impacts of pH and irradiation power on the drug release of Fe_3O_4@SiO_2@Au@porous SiO_2-DOX are studied. Finally, the toxicity of Fe_3O_4@SiO_2@Au@porous SiO_2 and Fe_3O_4@SiO_2@Au@porous SiO_2-DOX are studied through in vitro 3-(4,5-Dimethylthiazol-2-yl)-2,5-diphenyltetrazolium bromide (MTT) cell viability assay.

Experiment

Synthesis of Fe_3O_4@SiO_2@Au

Fe_3O_4 nanoparticles were synthesized through hydrolysis reaction at 220°C.[35] SiO_2 was coated on Fe_3O_4 particles through a modified Stober method. Specifically, Fe_3O_4 (0.1 g) was mixed in ethanol (100 mL) and ammonia solution (28%, 5 mL) with mechanical stirring. Tetraethyl orthosilicate (0.1 mL) was introduced into the solution every 10 minutes until the total volume reaches 1 mL. After cleaning with ethanol and DI water, the particles with SiO_2 layer of ~ 20 nm were dispersed in isopropanol (80 mL) and 3-aminopropyl-triethoxysilane (APTS, 200 μL) at 75°C for 1 hour so that the amino groups could be grafted to SiO_2 surface. Separately, the Au nanoparticles were synthesized through a Turkevich synthesis.[36] Fe_3O_4@SiO_2@Au particles were synthesized by mixing amine group–modified Fe_3O_4@SiO_2 nanoparticles with Au nanoparticles in DI water under ultrasonication. The mass ratio of Fe_3O_4@SiO_2 to Au was 20 to 1.

Synthesis of Fe_3O_4@SiO_2@Au@SiO_2

Another layer of SiO_2 was coated on Fe_3O_4@SiO_2@Au surface by a sol-gel method.[37] Briefly, Fe_3O_4@SiO_2@Au (0.1 g) and polyvidone (PVP, $(C6H9NO)_n$, 1 g, molecular weight [Mw]: $\sim 60\,000$) were mixed in 100 mL water and ultrasonicated for 10 minutes so that the polymer could be adsorbed on the surface of the particles. The colloids were then washed with DI water and introduced into a solution of ethanol (100 mL) and ammonia solution (28%, 5 mL). Tetraethyl orthosilicate (0.1 mL) was introduced into the dispersion every 10 minutes until

the total volume reaches 1 mL. Finally, Fe_3O_4@SiO_2@Au@SiO_2 nanoparticles with external SiO_2 layer of ~ 20 nm were obtained.

Synthesis of Fe_3O_4@SiO_2@Au@p-SiO_2

The external layer of SiO_2 in Fe_3O_4@SiO_2@Au@SiO_2 was etched into a porous structure so that Fe_3O_4@SiO_2@Au@p-SiO_2 could be prepared. Specifically, Fe_3O_4@SiO_2@Au@SiO_2 (0.1 g) and PVP (1 g, Mw: $\sim 10\,000$) were mixed in 100 mL DI water and refluxed at 100°C for 5 hours. After cooling down to room temperature, NaOH solution (0.32 g/mL, 5 mL) was introduced to the suspension under magnetic stirring. After stirring for 10 minutes, the solution pH was quickly regulated to 7 with dilute HCl to quench the etching reaction. The particles were washed with DI water, and Fe_3O_4@SiO_2@Au@p-SiO_2 particles were obtained.

Synthesis of Fe_3O_4@SiO_2@Au@p-SiO_2-DOX

Fe_3O_4@SiO_2@Au@p-SiO_2 particles (0.1 g) and DOX water solution (500 μg/mL, 50 mL) were stirred and shaken at room temperature for 24 hours in the dark. The final concentration of DOX could be determined by ultraviolet–visible (UV-Vis) spectroscopy. The loaded DOX could be calculated with the concentration difference.

Materials Characterization

The morphology of the particles was studied by transmission electron microscopy (TEM; Hitachi HT7700), and the crystal structure was determined by X-ray diffraction (XRD; Bruker D8). The surface area of the particles was investigated by N_2 adsorption–desorption isotherm curves. The existence of DOX on particle surface was determined by fluorescence spectroscopy (USB2000+; Ocean Optics).

Near-Infrared-Induced Drug Release With Fe_3O_4@SiO_2@Au@p-SiO_2-DOX

Near-infrared-induced DOX dry delivery and release were studied by the dialysis method. Briefly, Fe_3O_4@SiO_2@Au@p-SiO_2-DOX (40 mg) was filled in a dialysis bag, which was then exposed in a phosphate buffer saline (0.1 mol/L, 100 mL) at 37°C, and the pH was regulated based on the experimental design. The DOX-loaded system was exposed to NIR laser at 808 nm (P = 5, 7.5, and 10 W/cm^2) under stirring so that light–thermal conversion could be achieved. During the drug release, a sample solution (5 mL) was taken out every 25 minutes to determine the DOX concentration by UV-Vis spectroscopy. After the measurement, the sample solution was returned to the solution container.

In Vivo MTT Assay

C6 glioma cells were selected for cytotoxicity testing due to its wide availability and widely used for cytotoxicity
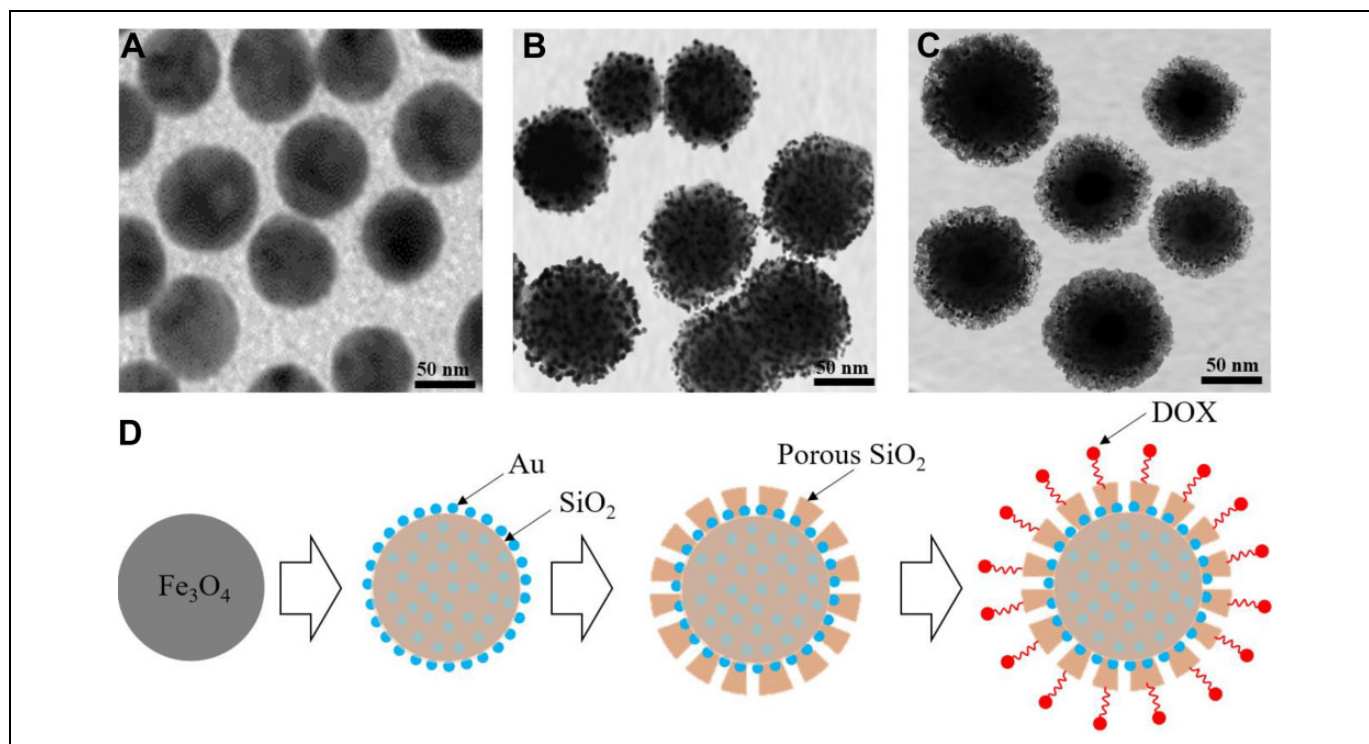
Figure 1. A, B, and D, Transmission electron microscopy (TEM) images for Fe3O4, Fe3O4@SiO2@Au, and Fe3O4@SiO2@Au@SiO2. D, Schematic for the synthesis procedure of Fe3O4@SiO2@Au@SiO2 doxorubicin (DOX).

investigation.[38] C6 glioma cells were seeded in a 96-well culture plate with 10% fetal bovine serum for 12 hours. The chamber was heated to 37°C and filled with 5% CO_2, and the cell density was controlled at 10 000 cells/well. The medium was 100 μL of Dulbecco Modified Eagle medium. Both DOX and $Fe_3O_4@SiO_2@Au@p-SiO_2$-DOX were dispersed in 100 mL culture medium, respectively, and then introduced into each well. Six wells without DOX or $Fe_3O_4@SiO_2@Au@p-SiO_2$-DOX were used as the control experiments. After incubation for 72 hours, the cytotoxicity was studied by MTT assay. The cell survival rate was calculated. The cytotoxicity of $Fe_3O_4@SiO_2@Au@p-SiO_2$ alone was also evaluated in a similar way.

Results and Discussion

The TEM image of Fe_3O_4 particles is presented in Figure 1A. It is observed that the particles are spherical, with a size around 50 nm. After coating a thin layer of SiO_2 and coupling agent of APTS on the surface of Fe_3O_4, Au nanoparticles were adsorbed on the SiO_2 surface due to the chemical interaction between Au and amine functional groups from APTS, and the corresponding TEM image of $Fe_3O_4@SiO_2@Au$ nanoparticles is presented in Figure 1B. With the presence of PVP, another layer of SiO_2 was coated on the outer layer of $Fe_3O_4@SiO_2@Au$ so that Au nanoparticles are fully encapsulated. Mesoporous structure of the outer SiO_2 is generated by protecting the near-surface layer of SiO_2 by PVP and etching the outer layer of SiO_2 in NaOH solution. Refluxing the particles in PVP solution results in the penetration of PVP into the SiO_2 surface by generating hydrogen bonds between carbonyl groups and silanol groups.[39] The polymer chains within SiO_2 could dramatically increase its stability in NaOH solution, while the regions without PVP protections would be easily etched by NaOH. Therefore, a porous structure of the outer SiO_2 layer is formed. Finally, $Fe_3O_4@-SiO_2@Au@p-SiO_2$ is synthesized, as shown in Figure 1C. A porous structured SiO_2 at the outer layer could provide a larger surface area for DOX loading. The general nanoparticle synthesis and DOX loading process are summarized in Figure 1D.

The porous nature of the outer SiO_2 layer could provide a larger surface area for DOX loading. To verify the surface area change before and after the formation of the porous structure, the N_2 adsorption/desorption curves for $Fe_3O_4@SiO_2@Au@SiO_2$ and $Fe_3O_4@SiO_2@Au@p-SiO_2$ are presented in Figure 2A. In $Fe_3O_4@SiO_2@Au@p-SiO_2$, the large hysteresis between adsorption and desorption curves indicates its porous structure. The specific surface area of $Fe_3O_4@SiO_2@Au@SiO_2$ and $Fe3O_4@SiO_2@Au@p-SiO_2$ is calculated as 87.5 and 143.5 m^2/g, respectively. It is observed that the porous structure could increase the specific surface area by 64%. The corresponding pore size distribution is presented in Figure 2B. The peak pore size is increased from 3.8 to 9.8 nm. Previous research shows that the diameter of DOX molecules is ~ 1.5 nm.[40] Therefore, the pore size is large enough to hold DOX molecules.

The electron paramagnetic resonance spectroscopy is used to study the magnetic properties of Fe_3O_4, $Fe_3O_4@SiO_2@Au$,
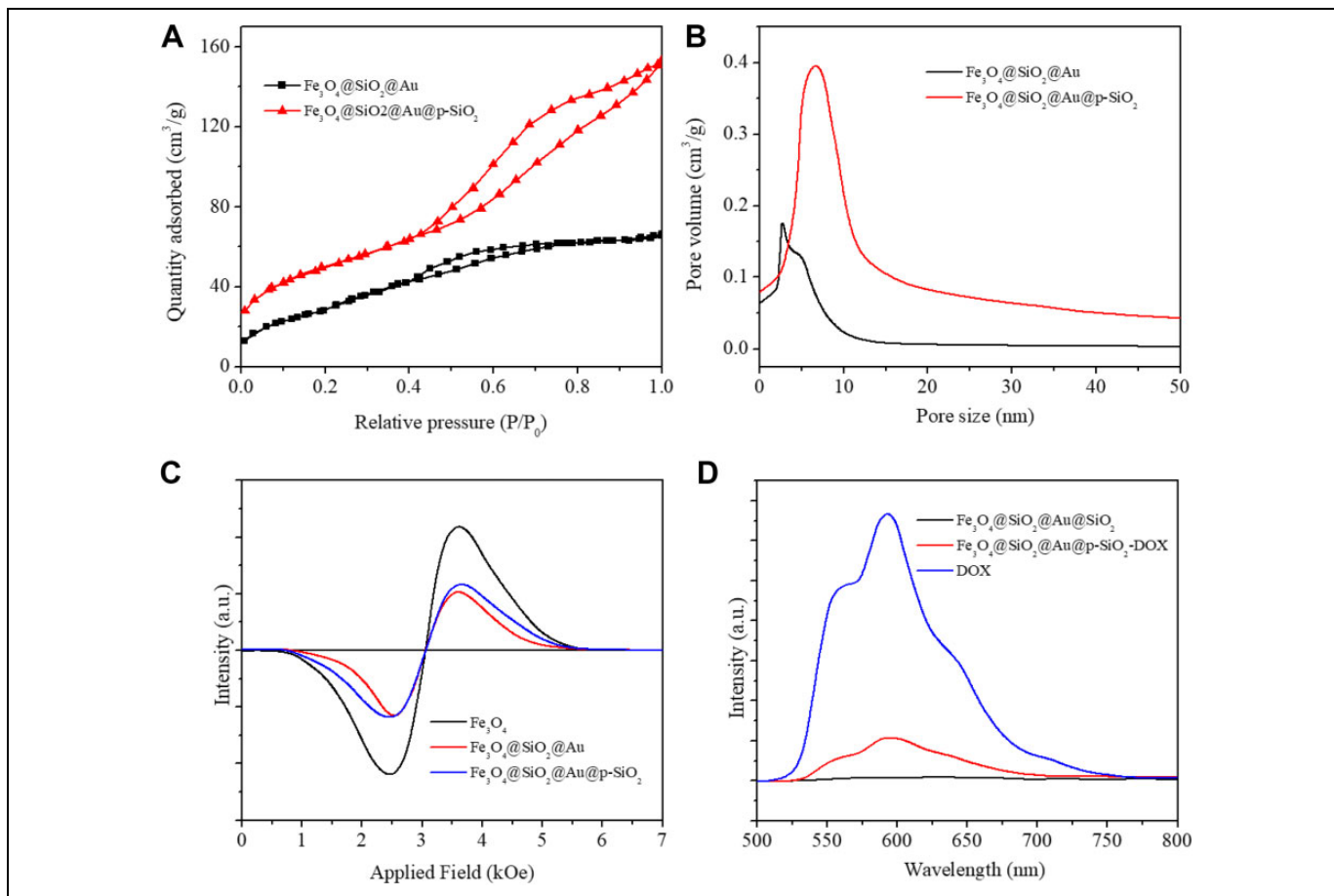
Figure 2. A, N2 adsorption/desorption curves for Fe3O4@SiO2@Au and Fe3O4@SiO2@Au@p-SiO2. B, Pore size distribution for Fe3O4@SiO2@Au and Fe3O4@SiO2@Au@p-SiO2. C, Electron paramagnetic resonance (EPR) spectra of Fe3O4, Fe3O4@SiO2@Au, and Fe3O4@SiO2@Au@p-SiO2. D, Fluorescence spectra of Fe3O4@SiO2@Au@p-SiO2 and Fe3O4, Fe3O4@SiO2@Au@p-SiO2-DOX, and doxorubicin (DOX).

and $Fe_3O_4@SiO_2@Au@p-SiO_2$, and the corresponding spectra are presented in Figure 2C. It shows that, after introducing different materials into Fe_3O_4, both peak intensity and width change, indicating the change in spin states within the particles, are attributed to the different environment of the magnetic phase, while the magnetization is still available within the composites, which is featured with the existence of peak in the spectra.

Fluorescence spectrum is applied to investigate the DOX loading behavior on $Fe_3O_4@SiO_2@Au@p-SiO_2$, and the corresponding fluorescence spectra for $Fe_3O_4@SiO_2@Au@p-SiO_2$ and $Fe_3O_4@Au@p-SiO_2$-DOX and DOX are presented in Figure 2A. Pure DOX shows a strong characteristic peak at around 600 nm. Meanwhile, $Fe_3O_4@SiO_2@Au@p-SiO_2$-DOX also shows a similar peak in a similar position, with a decreased intensity. This indicates that DOX is successfully introduced into $Fe_3O_4@SiO_2@Au@p-SiO_2$. As a reference and comparison, the fluorescence spectrum of $Fe_3O_4@SiO_2@Au@p-SiO_2$ is also presented in Figure 2D. It can be seen that there is no peak observed due to the absence of DOX.

The magnetic properties of Fe_3O_4, $Fe_3O_4@SiO_2@Au$, and $Fe_3O_4@SiO_2@Au@p-SiO_2$ are further characterized by VSM, and their magnetic hysteresis loops are presented in Figure 3A. It can be seen that pure Fe_3O_4 shows the highest magnetization of 47.3 emu/g, and $Fe_3O_4@SiO_2@Au$ and $Fe_3O_4@SiO_2@Au@p-SiO_2$ have the magnetization of 38.5 and 37.2 emu/g, respectively. The decreased magnetization could be attributed to the introduction of nonmagnetic phases, while the magnetization is still high enough to direct drug transportation.

The crystal structure of Fe_3O_4, $Fe_3O_4@SiO_2@Au$, and $Fe_3O_4@SiO_2@Au@p-SiO_2$ is studied by XRD, and the diffraction patterns are presented in Figure 3B. For pure Fe_3O_4, its diffraction peaks match well with that displayed in the JCPDS card (NO. 75-0033), indicating that Fe_3O_4 is well crystallized. Compared to Fe_3O_4, an extra Au peak (111) is observed in $Fe_3O_4@SiO_2@Au$ and $Fe_3O_4@SiO_2@Au@p-SiO_2$. This could be attributed to the introduction of Au nanoparticles. However, the peaks corresponding to SiO_2 nanoparticles are not detected. This is because SiO_2 synthesized by the Stober method is in the amorphous phase.
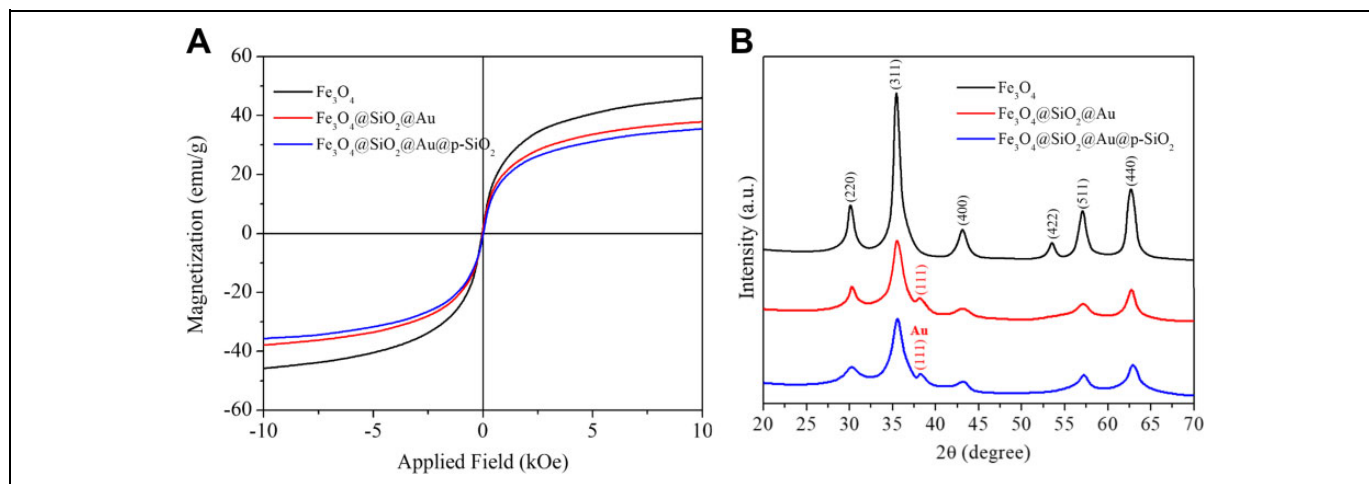
Figure 3. A, Magnetic hysteresis loops of Fe3O4, Fe3O4@SiO2@Au, and Fe3O4@SiO2@Au@p-SiO2. B, X-ray diffraction (XRD) patterns for Fe3O4, Fe3O4@SiO2@Au, and Fe3O4@SiO2@Au@p-SiO2.
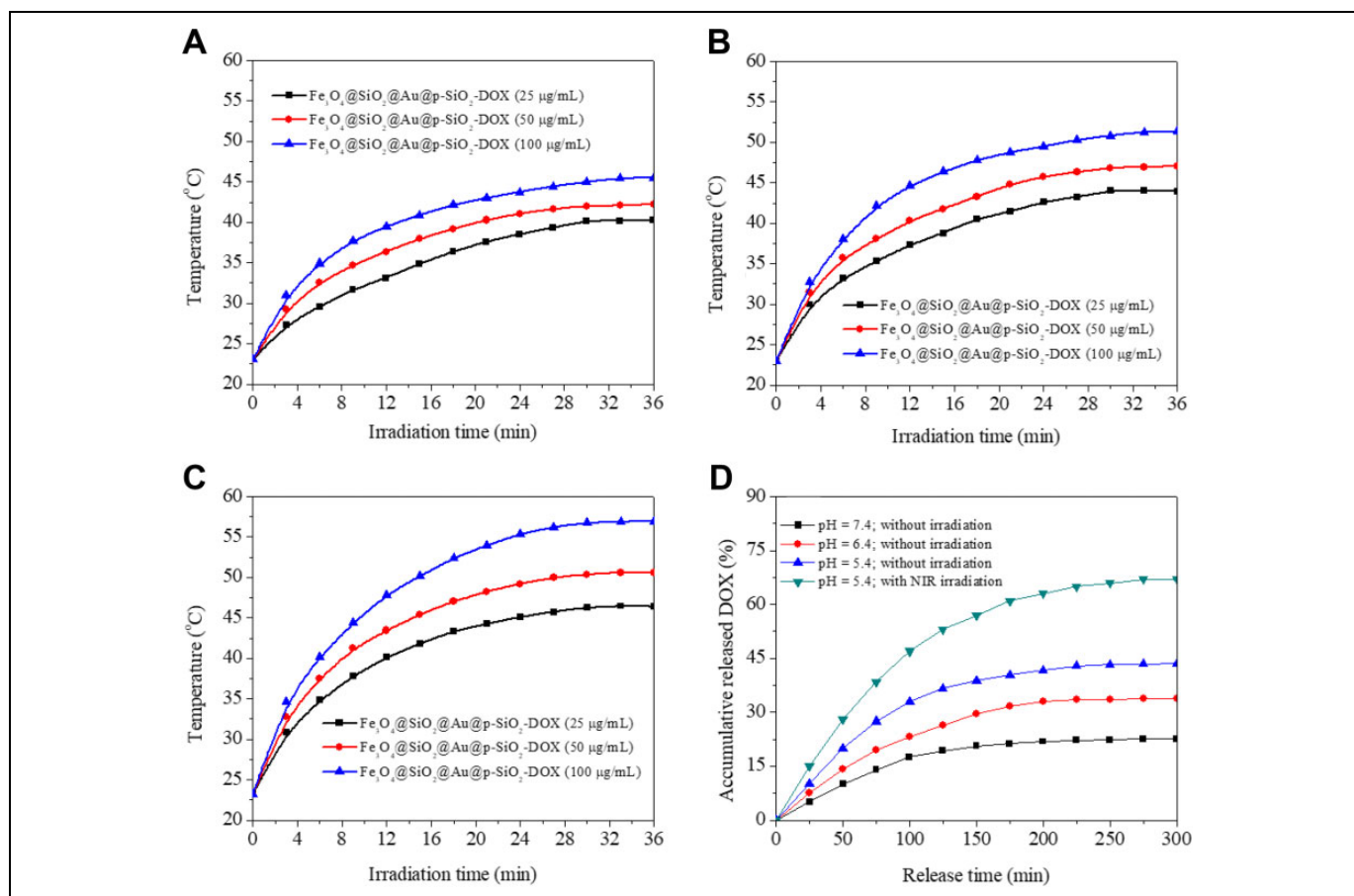

Figure 4. A-C, Temperature variation curves of Fe3O4@SiO2@Au@p-SiO2-DOX (25, 50, and 100 μg/mL) under 5, 7.5, and 10 W/cm^2 (the starting temperature was room temperature (23°C, pH = 7), the irradiation time was 36 minutes, and the temperature was measured every 3 minutes). D, Accumulative doxorubicin (DOX) released from various pH solutions and irradiation conditions (starting temperature of 37°C, Fe3O4@SiO2@Au@p-SiO2-DOX concentration of 25 μg/mL, and layer power of 10 W/cm^2).

To investigate the application of NIR-induced drug release, the temperature under different power of laser and irradiation time is presented in Figure 4A-C. In each experiment, the $Fe_3O_4@SiO_2@Au@p\text{-}SiO_2$-DOX concentration is controlled as 25, 50, and 100 μg/mL. Under a specific laser power, it is observed that a higher concentration of
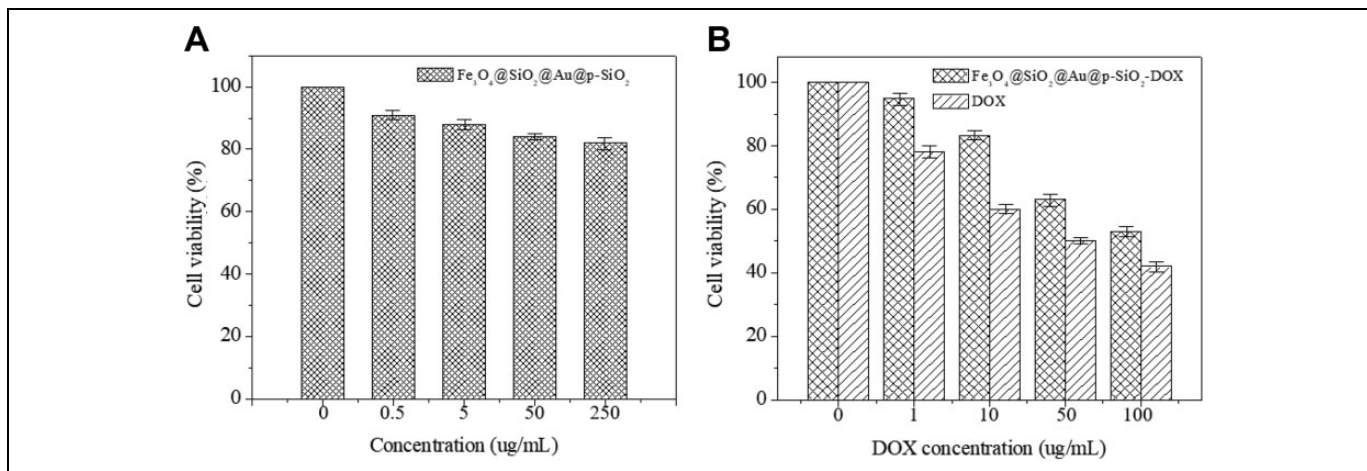
Figure 5. Results from in vitro cytotoxicity experiment. A, C6 cell viability after being incubated with different concentrations of $Fe_3O_4@$-$SiO_2@Au@p$-SiO_2 for 72 hours. B, C6 cell viability after being incubated with different concentrations of doxorubicin (DOX) and $Fe_3O_4@$-$SiO_2@Au@p$-SiO_2-DOX for 72 hours.

$Fe_3O_4@SiO_2@Au@p$-SiO_2-DOX results in a higher temperature. This could be attributed to the enhanced concentration of $Fe_3O_4@SiO_2@Au@p$-SiO_2-DOX which absorbs greater NIR light and therefore generates more heat. This also indicates that Au nanoparticles within $Fe_3O_4@SiO_2@Au@p$-SiO_2-DOX could quickly convert the photon energy from the NIR irradiation into heat. Besides, when the NIR power is increased, the corresponding temperature is also increased. This is because more irradiation energy is supplied to $Fe_3O_4@SiO_2@Au@p$-SiO_2-DOX, and therefore, more heat is generated. This result demonstrates that $Fe_3O_4@SiO_2@Au@p$-SiO_2 platform is suitable for the delivery and controlled release of drugs under NIR irradiation.

The impacts of pH on DOX release is also studied, and the results are presented in Figure 4D. First, the DOX release is studied under different pH without NIR irradiation, and the pH is controlled as 5.4, 6.4, and 7.4. It is observed that the DOX release is fast at the earlier stage and then slows down gradually. After releasing for 300 minutes, the accumulative DOX release reaches 18.3%, 31.2%, and 37.7% under the pH of 7.4, 6.4 and 5.4, respectively. This result indicates that a lower pH is beneficial for the fast delivery of DOX with the platform of $Fe_3O_4@SiO_2@Au@p$-SiO_2. This discovery could be used to guide the local pH regulation when releasing DOX into tumor tissue in the pathological process.

After that, NIR irradiation (10 W/cm^2) is applied to $Fe_3O_4@SiO_2@Au@p$-SiO_2-DOX release under the pH of 5.4. After 300 minutes of irradiation, the accumulative DOX release reaches 65.3%, which is almost twice of the condition without NIR irradiation. This result concludes that NIR irradiation plays a critical role in releasing DOX from $Fe_3O_4@SiO_2@Au@p$-SiO_2 platform.

As a platform for drug delivery and release, its toxicity needs to be well evaluated, which is performed through standard MTT cell viability assay. As shown in Figure 5A, the cytotoxicity of $Fe_3O_4@SiO_2@Au@p$-SiO_2 is impacted by its concentration but is generally limited. The C6 cell

viability could be maintained as high as $\sim 80\%$ when $Fe_3O_4@SiO_2@Au@p$-SiO_2 concentration is 250 µg/mL. It is concluded that $Fe_3O_4@SiO_2@Au@p$-SiO_2 does not have appreciable toxicity to C6 cells even after the incubation for 72 hours. The cytotoxicity of DOX and $Fe_3O_4@SiO_2@Au@p$-SiO_2-DOX with different concentrations in C6 cells is tested and presented in Figure 4B. Generally, $Fe_3O_4@SiO_2@Au@p$-SiO_2-DOX has lower toxicity than pure DOX. This is could be attributed to the loading ratio in $Fe_3O_4@SiO_2@Au@p$-SiO_2-DOX (the mass ratio of $Fe_3O_4@SiO_2@Au@p$-SiO_2), and the real DOX concentration in $Fe_3O_4@SiO_2@Au@p$-SiO_2-DOX experiment is much lower than that in pure DOX. In $Fe_3O_4@SiO_2@Au@p$-SiO_2-DOX experiment, even when its concentration reaches 100 µg/mL, the C6 cell viability could be maintained as high as $\sim 50\%$, indicating its relatively low toxicity to the cells.

Conclusions

$Fe_3O_4@SiO_2@Au@p$-SiO_2 nanoparticles were synthesized, and DOX was attached to the particle surface. The BET method study indicated that the particles have a porous structure, which was beneficial to load DOX. The drug delivery and release were studied under NIR irradiation. The impacts of laser power and environmental pH on drug delivery and release were investigated. The study indicated that a lower pH and higher power of laser were beneficial for DOX drug release. Finally, the cytotoxicity of both $Fe_3O_4@SiO_2@Au@p$-SiO_2 and $Fe_3O_4@$-$SiO_2@Au@p$-SiO_2-DOX was studied through in vitro MTT assay with C6 glioma cells. The results indicated that both $Fe_3O_4@$-$SiO_2@Au@p$-SiO_2 and $Fe_3O_4@SiO_2@Au@p$-SiO_2-DOX have limited cytotoxicity to the cells.

Declaration of Conflicting Interests

ORCID iD

Dongliang Shi ⬤ https://orcid.org/0000-0002-2200-9335

References

1. Peer D, Karp JM, Hong S, Farokhzad OC, Margalit R, Langer R. Nanocarriers as an emerging platform for cancer therapy. *Nat Nanotechnol*. 2007;2(12):751-760.

2. Kang L, Zhao L, Yao S, Duan C. A new architecture of superhydrophilic β-SiAlON/graphene oxide ceramic membrane for enhanced anti-fouling and separation of water/oil emulsion. *Ceram Int*. 2019;45(13):16717-16721.

3. Zhang Q, Bolisetty S, Cao Y, et al. Selective and efficient removal of fluoride from water: in situ engineered amyloid fibril/ZrO2 hybrid membranes. *Angew Chem Int Ed*. 2019;58(18):6012-6016.

4. Chen H, Zhang S, Zhao Z, Liu M, Zhang Q. Application of dopamine functional materials in water pollution control. *Prog Chem*. 2019;31(4):571-579.

5. Huang C-Y, Ju D-T, Chang C-F, Muralidhar Reddy P, Velmurugan BK. A review on the effects of current chemotherapy drugs and natural agents in treating non–small cell lung cancer. *Biomedicine*. 2017;7(4):23.

6. Niu L, Xu J-L, Yang W-L, Kang C-H, Ma J-Q, Su J-Q. Synergistic effect between nano-Sb2O3 and brominated epoxy resin on the flame retardancy of poly(butylene terephthalate). *Sci Adv Mater*. 2019;11(4):466-475.

7. Yuan D, Zhang C, Tang S, et al. Enhancing CaO2 fenton-like process by Fe(II)-oxalic acid complexation for organic wastewater treatment. *Water Res*. 2019;163:114861.

8. Hussain A, Guo S. NIR-triggered release of DOX from sophorolipid-coated mesoporous carbon nanoparticles with the phase-change material 1-tetradecanol to treat MCF-7/ADR cells. *J Mater Chem B*. 2019;7(6):974-985.

9. Shen S, Huang D, Cao J, et al. Magnetic liposomes for light-sensitive drug delivery and combined photothermal–chemotherapy of tumors. *J Mater Chemi B*. 2019;7(7):1096-1106.

10. Chen W, Chang L, Ren S-B, He Z-C, Huang G-B, Liu X-H. Direct Z-scheme 1D/2D WO2.72/ZnIn2S4 hybrid photocatalysts with highly-efficient visible-light-driven photodegradation towards tetracycline hydrochloride removal. *J Hazard Mater*. 2020;384:121308.

11. Qiao X, Zhao C, Shao Q, Hassan M. Structural characterization of corn stover lignin after hydrogen peroxide presoaking prior to ammonia fiber expansion pretreatment. *Energy Fuels*. 2018;32(5):6022-6030.

12. Zhao C, Qiao X, Cao Y, Shao Q. Application of hydrogen peroxide presoaking prior to ammonia fiber expansion pretreatment of energy crops. *Fuel*. 2017;205:184-191.

13. Zhang H, Fang Y. Temperature dependent photoluminescence of surfactant assisted electrochemically synthesized ZnSe nanostructures. *J Alloy Compd*. 2019;781:201-208.

14. Tang S, Li N, Yuan D, et al. Comparative study of persulfate oxidants promoted photocatalytic fuel cell performance: simultaneous dye removal and electricity generation. *Chemosphere*. 2019;234:658-667.

15. Kanwal U, Irfan Bukhari N, Ovais M, Abass N, Hussain K, Raza A. Advances in nano-delivery systems for doxorubicin: an updated insight. *J Drug Target*. 2018;26(4):296-310.

16. Tiwari G, Tiwari R, Sriwastawa B, et al. Drug delivery systems: an updated review. *Int J Pharm Investig*. 2012;2(1):2-11.

17. Jahangirian H, Lemraski EG, Webster TJ, Rafiee-Moghaddam R, Abdollahi Y. A review of drug delivery systems based on nanotechnology and green chemistry: green nanomedicine. *Int J nanomed*. 2017;12:2957-2978.

18. Zhao C, Cao Y, Ma Z, Shao Q. Optimization of liquid ammonia pretreatment conditions for maximizing sugar release from giant reed (Arundo donax L.). *Biomass Bioenergy*. 2017;98(2):61-69.

19. Zhao C, Shao Q, Ma Z, Li B, Zhao X. Physical and chemical characterizations of corn stalk resulting from hydrogen peroxide presoaking prior to ammonia fiber expansion pretreatment. *Ind Crop Prod*. 2016;83:86-93.

20. Du H, Ma C, Ma W, Wang H. Microstructure evolution and dielectric properties of Ce-doped SrBi4Ti4O15 ceramics synthesized via glycine-nitrate process. *Process Appl Ceram*. 2018;12(4):303-312.

21. Yuan D, Sun M, Tang S, et al. All-solid-state BiVO4/ZnIn2S4 Z-scheme composite with efficient charge separations for improved visible light photocatalytic organics degradation. *Chin Chem Lett*. 2019;31(2):547-550. doi:10.1016/j.cclet.2019.09.051.

22. Duan C, Cao Y, Hu L, Fu D, Ma J, Youngblood J. An efficient mechanochemical synthesis of alpha-aluminum hydride: synergistic effect of TiF3 on the crystallization rate and selective formation of alpha-aluminum hydride polymorph. *J Hazard Mater*. 2019;373:141-151.

23. Riley RS, Day ES. Gold nanoparticle-mediated photothermal therapy: applications and opportunities for multimodal cancer treatment. *Wiley Interdisc Rev Nanomed Nanobiotechnol*. 2017;9(4).

24. Jang Y, Lee N, Kim JH, Park YI, Piao Y. Shape-controlled synthesis of au nanostructures using EDTA tetrasodium salt and their photothermal therapy applications. *Nanomaterials (Basel, Switzerland)*. 2018;8(4):E252.

25. Liu S-Y, Liang Z-S, Gao F, Luo S-F, Lu G-Q. In vitro photothermal study of gold nanoshells functionalized with small targeting peptides to liver cancer cells. *J Mater Sci Mater Med*. 2010;21(2):665-674.

26. Paasonen L, Laaksonen T, Johans C, Yliperttula M, Kontturi K, Urtti A. Gold nanoparticles enable selective light-induced contents release from liposomes. *J Control Release*. 2007;122(1):86-93.

27. Angelatos AS, Radt B, Caruso F. Light-responsive polyelectrolyte/gold nanoparticle microcapsules. *J Phys Chem B*. 2005;109(7):3071-3076.

28. Hassan M, Umar M, Ding W, Mehryar E, Zhao C. Methane enhancement through co-digestion of chicken manure and oxidative cleaved wheat straw: stability performance and kinetic modeling perspectives. *Energy*. 2017;141:2314-2320.

29. Zhao C, Ma Z, Shao Q, Li B, Ye J, Peng H. Enzymatic hydrolysis and physiochemical characterization of corn leaf after H-AFEX pretreatment. *Energy Fuels*. 2016;30(2):1154-1161.

30. Liu D, Cao Y, Liu J, Gao Y, Wang Y. Effect of oxygen partial pressure on temperature for onset of flash sintering 3YSZ. *J Eur Ceram Soc*. 2018;38(2):817-820.

31. Liu X, Tao Y, Mao H, et al. Construction of magnetic-targeted and NIR irradiation-controlled drug delivery platform with Fe3O4@Au@SiO2 nanospheres. *Ceram Int*. 2017;43(6): 5061-5067.

32. Zhao C, Shao Q, Li B, Ding W. Comparison of hydrogen peroxide and ammonia pretreatment of corn Stover: solid recovery, composition changes, and enzymatic hydrolysis. *Energy Fuels*. 2014; 28(10):6392-6397.

33. Liu G, Liu D, Liu J, Gao Y, Wang Y. Asymmetric temperature distribution during steady stage of flash sintering dense zirconia. *J Eur Ceram Soc*. 2018;38(7):2893-2896.

34. Liu X, Zhao Y, Shi J, et al. Improvement of dielectric and ferroelectric properties in bismuth sodium titanate based relaxors through Bi non-stoichiometry. *J Alloy Compd*. 2019;799:231-238.

35. Ge JP, Hu YX, Biasini M, Beyermann WP, Yin YD. Superparamagnetic magnetite colloidal nanocrystal clusters. *Angew Chem Int Edit*. 2007;46(23):4342-4345.

36. Turkevich J, Stevenson PC, Hillier J. A study of the nucleation and growth processes in the synthesis of colloidal gold. *Discuss Faraday Soc*. 1951;11:55-75.

37. Graf C, Vossen DLJ, Imhof A, Van Blaaderen A. A general method to coat colloidal particles with silica. *Langmuir*. 2003; 19(17):6693-6700.

38. Song M-M, Xu H-L, Liang J-X, Xiang H-H, Liu R, Shen Y-X. Lactoferrin modified graphene oxide iron oxide nanocomposite for glioma-targeted drug delivery. *Mater Sci Eng C*. 2017;77: 904-911.

39. Gun'ko VM, Zarko VI, Voronin EF, et al. Successive interaction of pairs of soluble organics with nanosilica in aqueous media. *J Colloid Interf Sci*. 2006;300(1):20-32.

40. Bilalis P, Tziveleka L, Varlas S, Iatrou H. pH-sensitive nanogates based on poly(l-histidine) for controlled drug release from mesoporous silica nanoparticles-ESI. *Polymer Chemistry*. 2016;7(7): 1475-1485.